Functional electronic inversion layers at ferroelectric domain walls

J. A. Mundy[1,*], J. Schaab[2,*], Y. Kumagai[2,*], A. Cano[3], M. Stengel[4,5], I. P. Krug[6], D. M. Gottlob[7], H. Doganay[7], M. E. Holtz[1], R. Held[8], Z. Yan[9,10], E. Bourret[9], C. M. Schneider[7], D. G. Schlom[8,11], D. A. Muller[1,11], R. Ramesh[9,12], N. A. Spaldin[2], and D. Meier[2,13,#]

*These authors contributed equally to this work

#dennis.meier@ntnu.no

[1] School of Applied and Engineering Physics, Cornell University, Ithaca, New York 14853, USA

[2] Department of Materials, ETH Zürich, CH-8093 Zurich, Switzerland

[3] CNRS, Université de Bordeaux, ICMCB, UPR 9048, 33600 Pessac, France

[4] ICREA—Institució Catalana de Recerca i Estudis Avançats, 08010 Barcelona, Spain

[5] Institut de Ciència de Materials de Barcelona (ICMAB-CSIC), Campus UAB, 08193 Bellaterra, Spain

[6] Institut für Optik und Atomare Physik, TU Berlin, 10623 Berlin, Germany

[7] Peter Grünberg Institute (PGI-6), Forschungszentrum Jülich, 52425 Jülich, Germany

[8] Department of Materials Science and Engineering, Cornell University, Ithaca, New York 14853, USA

[9] Materials Sciences Division, Lawrence Berkeley National Laboratory, Berkeley, California 94720, USA

[10] Department of Physics, ETH Zurich, Otto-Stern-Weg 1, 8093 Zurich, Switzerland

[11] Kavli Institute at Cornell for Nanoscale Science, Ithaca, New York 14853, USA

[12] Department of Materials Science and Engineering and Department of Physics, UC Berkeley, Berkeley, California 94720, USA

[13] Department of Materials Science and Engineering, Norwegian University of Science and Technology, 7491 Trondheim, Norway

Ferroelectric domain walls hold great promise as functional 2D-materials because of their unusual electronic properties. Particularly intriguing are the so-called charged walls where a polarity mismatch causes local, diverging electrostatic potentials requiring charge compensation and hence a change in the electronic structure. These walls can exhibit significantly enhanced conductivity and serve as a circuit path. The development of *all-domain-wall* devices, however, also requires walls with controllable output to emulate electronic nano-components such as diodes and transistors. Here we demonstrate electric-field control of the electronic transport at ferroelectric domain walls. We reversibly switch from resistive to conductive behavior at charged walls in semiconducting $ErMnO_3$. We relate the transition to the formation – and eventual activation – of an inversion layer that acts as the channel for the charge transport. The findings provide new insight to the domain-wall physics in ferroelectrics and foreshadow the possibility to design elementary digital devices for all-domain-wall circuitry.

Recently, ferroelectric domain walls have been demonstrated to develop novel electronic ground states that differ from those of the surrounding bulk material. In addition, they can be induced, moved, and erased on demand, representing natural, flexible interfaces with novel functional properties[1-3]. After the seminal discovery of electrically conducting walls in the multiferroic semiconductor $BiFeO_3$[4], there have been numerous reports on conducting walls in prototypical ferroelectrics including $PbZr_{0.2}Ti_{0.8}O_3$[5], $LiNbO_3$[6], and $BaTiO_3$[7], as well as improper ferroelectrics such as hexagonal RMnO$_3$ (R = Sc, Y, In, Dy to Lu)[8,9] and $(Ca,Sr)_3Ti_2O_7$[10], indicating that such conductivity is a general phenomenon[2,3,11,12]. Conducting domain walls are now anticipated in a wide range of otherwise insulating ferroic materials, with the observation of metallic domain walls in the magnetic insulator $Nd_2Ir_2O_7$ being a major new development[13]. Furthermore, recently established characterization methods allow to determine intrinsic domain wall properties with unprecedented completeness. Local Hall measurements, for instance, reveal the types, mobilities and densities of involved carriers[14], and advanced frequency-dependent[15,16] and contact-free transport[17,18] measurements provide insight into the underlying conduction mechanisms. In order to make use of the exotic domain wall properties and ultimately design domain-wall-based devices for nanotechnology, however, additional functionality beyond just conduction is required that allows the behavior of classical electrical components to be emulated at the nanoscale. Here, we demonstrate electric-field control of the electronic transport at charged head-to-head domain walls in semiconducting $ErMnO_3$. The electric field allows reversible switching between resistive and conductive domain wall states,

72 corresponding to a domain-wall-based binary switch. We relate this qualitative change
73 in the transport behavior to the formation – and eventual activation – of an electronic
74 inversion layer at the head-to-head walls that acts as the channel for the charge
75 transport.

76 For our study we choose the narrow band gap, p-type semiconductor $ErMnO_3$ (E_g
77 = 1.6 eV[19]) as it naturally develops all fundamental types of ferroelectric domain walls at
78 room temperature (T_C = 1470 K[20]), including neutral (side-by-side) as well as negatively
79 (tail-to-tail) and positively charged (head-to-head) wall configurations[8]. Moreover, the
80 atomic structure and basic transport properties of these walls are particularly well-
81 understood[8,21,22]. While the main interest in neutral domain walls is associated with
82 their functionality as insulating barriers[23], charged domain walls are intriguing because
83 of their unique electrostatics, giving rise to diverse and tunable electronic transport
84 properties[8]. Enhanced electronic conductance has been reported for tail-to-tail walls in
85 $ErMnO_3$ and explained based on the accumulation of mobile holes[3,14]. The holes
86 originate from interstitial oxygen anions[24] and represent the majority carriers. These
87 carriers accumulate at tail-to-tail walls to screen the local, divergent electric field.
88 Likewise, head-to-head walls in the same sample exhibit suppressed conductance, which
89 has been explained by the depletion of majority carriers, with possible additional
90 contributions from minority carriers (electrons)[8,11]. The latter are particularly interesting,
91 as the involvement of both majority and minority carriers may give rise to novel,
92 functional domain-wall behavior.

93 In order to study emergent domain-wall properties at head-to-head walls in
94 $ErMnO_3$, we measure the local electronic transport over an extended voltage range.
95 Crystals of $ErMnO_3$ were grown by the pressurized floating-zone method[25] and
96 specimens with in-plane polarization and a thickness of ≈ 1 mm were prepared and
97 chemo-mechanically polished with silica slurry. In Fig. 1a–c we present conductive
98 atomic force microscopy (cAFM) data obtained with a conductive diamond-coated tip
99 (DCP12, NT-MDT) under sample bias voltages of up to 6 V. Test measurements on
100 different walls and with different tip-coatings reveal bulk-dominated transport behavior,
101 ensuring that intrinsic domain wall properties are probed (see Supplementary Notes and
102 Supplementary Fig. 1 and 2). At low bias voltage (V_{bias} = 2.5 V) we observe the
103 established transport behavior[8,9] with conducting tail-to-tail (bright) and insulating
104 head-to-head (dark) domain walls (Fig. 1a). A qualitatively different transport
105 phenomenon, however, arises at higher voltage as shown by the scan in Fig. 1b, taken at
106 V_{bias} = 6 V. The spatially resolved data highlights that both tail-to-tail and head-to-head
107 walls can exhibit a higher electronic conductance than the surrounding domains. A more
108 detailed study is shown in Fig. 1c, which is conducted in an area with well-separated
109 walls to exclude crosstalk effects (see Supplementary Figure 3). Figure 1c shows the
110 relative domain-wall conductance, ΔI, after subtracting the bulk current, which for
111 reference, is shown in the inset to Fig. 1c ($\Delta I = I_{wall} - I_{bulk}$). The comparison with respect
112 to the bulk (black dotted line in Fig. 1c) reveals that the head-to-head domain walls
113 become more conducting than the bulk above $V_c \approx 4.8$ V, approaching the conductance
114 measured at the tail-to-tail walls for $V > V_c$. The transition from resistive ($I_{wall} < I_{bulk}$) to

115 conductive (I_{wall} > I_{bulk}) behavior occurs gradually and for moderate electric fields (see
116 also Supplementary Fig. 2). For comparison, more than one order of magnitude higher
117 electric fields are used to induce domain wall currents in $BiFeO_3$ or $PbZr_{0.2}Ti_{0.8}O_3$ thin
118 films[4,5]. The low electric field energy suggests a *qualitative* change in the electronic
119 transport at head-to-head walls rather than a breakdown of the insulating domain wall
120 state. This qualitative change, however, cannot be explained based on the depletion of
121 majority carriers (holes) alone.

122 To better understand this unusual transport phenomenon, we build a DFT-based
123 semi-classical model describing the redistribution of mobile carriers. Assuming that
124 $ErMnO_3$ behaves like a simple band insulator we solve Poisson`s equation self-
125 consistently with the carriers treated semi-classically (see Methods for details) and
126 obtain the band diagram presented in Fig. 1d. We see that far from the domain walls the
127 potential is flat and the Fermi level, E_{Fermi}, lies just below the valence-band maximum
128 (VBM) corresponding to a realistic carrier density of $p_0 = 2 \cdot 10^{19}$ cm^{-3}, i.e., a doping level
129 of 0.007 holes per unit cell. At the tail-to-tail walls the VBM shifts upwards and
130 generates more holes which screen the negative bound domain-wall charge, $-2P_z$ ($\mathbf{P} = (0,$
131 $0, P_z)$); this is consistent with the enhanced conductance measured at the tail-to-tail
132 domain walls[8,9] (see Fig. 1a). For the head-to-head domain walls, we find a significant
133 band bending with the conduction-band minimum (CBM) dipping below the Fermi
134 energy. This implies that the screening at head-to-head domain walls is realized by both
135 a depletion of holes, occurring in a total range of about 22 nm, and an accumulation of
136 electrons right at the wall where the CBM lies below E_{Fermi} (see Fig. 1d). Thus, the simple

137 model indicates that the density of electrons, i.e., the minority carriers, is considerably
138 enhanced at the head-to-head walls. This result is in agreement with previous analytical
139 investigations[11], demonstrating the soundness of our alternative DFT-based approach. In
140 both models, however, hole depletion needs to override the electron accumulation in
141 order to reproduce the experimental observation of insulating walls for $V < V_c$ (Fig. 1a).
142 The latter is illustrated in Fig. 1e, where the density of carriers is plotted as a function of
143 the distance from the wall. The corresponding average carrier density – which is
144 proportional to the conductance – is shown in the inset. For $V > V_c$ the electrons likely
145 dominate the domain-wall conductance as they are the only mobile carriers available for
146 charge transport at the head-to-head walls. Aside from the observed change in
147 conductance, the pronounced band bending at head-to-head walls is appealing for the
148 design of domain-wall-based transistors as sketched in Fig. 1f. The field effect associated
149 with the polarization charges can, in principle[8,26], be used to modulate the conductivity
150 at the wall and, hence, serve as a natural, intrinsic gate. In the following, however, we
151 will focus on the voltage-driven transition from resistive to conductive behavior.

152 We next use electron energy loss spectroscopy (EELS) to probe the electronic
153 structure at the head-to-head walls at atomic resolution. Figure 2a shows a high-angle
154 annular dark field scanning transmission electron microscopy (HAADF-STEM) image of a
155 head-to-head domain wall imaged along the [100] zone axis of $ErMnO_3$ (see Methods for
156 details). The erbium ions are shifted with respect to the manganese-oxygen polyhedra,
157 displaying either an up-down-down (–*P* domain) or down-up-up (+*P* domain)
158 arrangement[21]. These displacements indicate the local spontaneous polarization and

159 thus provide a local measure for the polarization reorientation across the head-to-head
160 wall. We find a rather abrupt discontinuity of the polarization orientation at the wall,
161 consistent with previous work[21]. Using spatially resolved EELS we investigate the
162 electrochemical wall structure by measuring the local manganese valence. Figure 2b
163 displays the evolution of the corresponding EELS spectra, taken at the Mn $L_{2,3}$-edge,
164 across the head-to-head wall. Figure 2c shows an enlarged image of the Mn L_3-edge
165 where the experimental data points are overlaid with a manganese reference spectrum
166 collected on the $ErMnO_3$ sample away from the domain wall. The spectra collected
167 within the domain areas exhibit minor differences that reflect an inhomogeneity of the
168 electrical background. In the vicinity of the head-to-head wall, we clearly note a distinct
169 feature at ~641 eV in the spectra. Here, the data is not well described by the Mn^{3+}
170 reference spectrum (see also Supplementary Figure 4).

171 To quantify the change observed at the Mn $L_{2,3}$-edge at the head-to-head wall,
172 the full Mn $L_{2,3}$-edge is fitted with two spectra corresponding to the Mn^{3+} and $Mn^{2.8+}$
173 valence states. The $Mn^{2.8+}$ spectrum is calculated as a linear combination of Mn^{3+} and
174 Mn^{2+} spectra as described in the Supplementary Notes and Supplementary Fig. 5 (we
175 note that the spectrum of six-fold coordinated Mn^{2+} is used for reference as the current
176 work represents the first spectroscopic study of the Mn^{2+} electronic state in trigonal
177 bipyramidal coordination). The analysis reveals a statistically significant concentration of
178 the lower valence state spatially localized over 2 - 3 unit cells near the head-to-head
179 domain wall. Based on the valence concentration, we calculate the excess charge per
180 manganese atom at the domain wall relative to the Mn^{3+} state in the bulk[27]. This charge

181 as a function of position is plotted in Fig. 2d. Aggregating over several such walls at
182 distinct locations in the material, we find that the local valence change is equivalent to
183 the accumulation of a negative charge of 0.09 ± 0.04 electrons per manganese atom at
184 the head-to-head wall position. Since the bulk polarization[28] of $ErMnO_3$ is $\approx 6\ \mu C/cm^2$,
185 the amount of negative charge density needed to screen the polar discontinuity at the
186 head-to-head walls is $\approx 12\ \mu C/cm^2$. This value converts into a carrier density in the order
187 of ≈ 0.1 (0.3) electrons per manganese ion (unit cell, u.c.), which is in the range of our
188 experimental uncertainty. Complementary EELS measurements at the oxygen K-edge
189 show no statistically relevant anomaly (Supplementary Fig. 5c), excluding that oxygen
190 vacancy formation is responsible for the local manganese valence change. EELS studies
191 at tail-to-tail walls and X-ray photoemission electron microscopy further confirm that
192 the lower valence state is a feature that is unique to the 2 – 3 unit cell wide area around
193 the head-to-head walls (see Supplementary Notes and Supplementary Fig. 6-8). In
194 agreement with our semi-classical model, the EELS results corroborate that electron
195 accumulation, in addition to hole depletion, plays an important role for the
196 compensation of the polarity mismatch at head-to-head domain walls in $ErMnO_3$.

197 To determine the orbital character of the electrons and elucidate the relation
198 between their accumulation and the local manganese valence state, we perform first-
199 principles calculations based on density functional theory (DFT) within the local density
200 approximation (LDA) $+U$ method using $YMnO_3$ as our model hexagonal manganite
201 ($YMnO_3$ is structurally and electronically similar to $ErMnO_3$, and the absence of f-
202 electrons simplifies the DFT description). In Fig. 3a we show the calculated orbital-

203 resolved density of states for the valence and conduction bands. We see that, consistent
204 with literature calculations[29,30], the conduction band is narrow because it is formed from
205 localized d_{z^2}-orbitals, with only minimal hybridization with neighboring axial oxygen p_z-
206 orbitals, whereas the valence band is broad, consisting of strongly hybridized and
207 delocalized manganese *d*- and oxygen 2*p*-states. At the head-to-head walls, where the
208 CBM dips below the Fermi level (Fig. 1d), we therefore expect localized electrons,
209 whereas holes at the VBM are delocalized in nature. This expectation is consistent with
210 our spectroscopy data, indicating a manganese valence change associated with the
211 accumulation of electrons.

212 While our theoretical analysis gives an appealing qualitative description of our
213 experimental data, at the quantitative level there is a discrepancy between the density
214 of electron carriers at the domain wall predicted by the semi-classical model and that
215 indicated by the EELS measurements. According to the cAFM measurements, hole
216 depletion needs to override the electron accumulation in the model, while EELS points
217 to a dominant electron-like compensation. This raises the question of whether an
218 additional mechanism is at play in the hexagonal manganites. The semi-classical model
219 and even our DFT band picture constitute a drastic simplification of the problem,
220 especially in a material such as $ErMnO_3$, where many-body correlation effects likely play
221 an important role. In this context, it is important to recognize that electrons in the
222 spatially localized manganese d_{z^2}-orbitals experience a strong on-site Coulombic
223 repulsion, which typically favors the formation of localized polaronic states rather than
224 itinerant Bloch states[31]. To verify whether such a scenario might apply to our case, we

225 calculate the energies of hypothetical polaronic states for both electrons and holes by
226 introducing a single electron or hole in a 120-atom supercell and lowering the local
227 symmetry around a manganese site (see Methods). We find (Fig. 3b) that an isolated
228 electron polaron has lower energy than an itinerant Bloch electron for U values of 7.5 eV
229 and higher. (In contrast, hole polarons remain unstable relative to the Bloch state even
230 for U values as large as 8.5 eV.) At head-to-head domain walls, we expect that polarons
231 arrange in a two-dimensional lattice, and thereby significantly reduce their formation
232 energy compared to the case of an isolated defect. We find that, by combining the latter
233 effect with the data of Fig. 3b and our band-bending model (see Supplementary
234 Information), polarons are most likely to form right at the head-to-head wall, for a
235 realistic range of values of both the Hubbard U ($U \approx$ 6-6.5 eV) and the bulk doping level.
236 Note that polarons should give an additional barrier to electronic conductivity at low
237 voltage, consistent with the observations presented in Fig. 1, lifting the band-model-
238 related condition that hole depletion dominates over electron accumulation at head-to-
239 head walls (Fig. 1e).

240 Thus, experiment and theory identify an accumulation of electrons at the head-
241 to-head walls, leading to the formation of an inversion layer. The electrons are in a
242 localized polaronic state and hence do not contribute to the conductance at low voltage.
243 For high voltage ($V > V_c$) these electrons dominate the conductance as they are the only
244 available mobile carriers. In the polaronic picture, V_c is related to the transition from
245 localized to itinerant electrons and hence to the activation of the inversion layer as the
246 effective channel for the domain-wall transport. This behavior is fundamentally different

247 from the majority-carrier-enabled transport at tail-to-tail domain walls, which does not
248 involve significant lattice coupling[14].

249 In Figure 4a,b we show how this behavior can be used in order to realize, e.g., a
250 domain-wall-based binary switch. The cAFM data in Fig. 4a is collected at a head-to-
251 head wall as a function of time with the bias voltage varying repeatedly between V_0 = 2
252 V and $V_0 + \Delta V$ = 5 V. Due to the unusual *I-V* characteristic at the head-to-head wall, the
253 change in electric field allows reversible switching between resistive ($I_0 < I_{bulk}$) and
254 conductive ($I_1 > I_{bulk}$) behavior as reflected by the normalized domain-wall current $1 / \Delta V$
255 $\cdot (\Delta I / I_{bulk})$ in Fig. 4a. Figure 4b shows that the related electric-field induced gain, $\Delta I / \Delta V$,
256 can be enhanced by increasing the base voltage V_0. The enhancement in gain, however,
257 is accompanied by the flow of a larger current I_0, which causes irreversible changes in
258 the electronic surface structure and fast degradation of the domain-wall-based binary
259 switch after only two to three cycles (not shown). Note that the transition from resistive
260 to conductive behavior reflects a change from hole- to electron-dominated conductance.
261 This qualitative change in the transport behavior is a unique feature of the inversion
262 layer formed at the head-to-head walls.

263 The head-to-head domain walls studied in this work thus represent a natural
264 type of semiconducting oxide interface at which the nature of the electronic transport
265 can be manipulated at will and in a fully reversible fashion. This new degree of freedom
266 becomes possible as the local transport behavior is determined by the interplay
267 between holes and electrons. Now that we have shown that functional inversion layers

268 are formed at charged domain walls, the next step is to utilize individual walls in device-
269 like architectures. In general, an involvement of both minority and majority carries is
270 appealing as it allows device paradigms to be extended into the realm of minority-
271 carrier devices including bistable switches and bipolar transistors. Minority-carrier
272 devices are typically slower, but offer better on-state performance and larger
273 breakdown voltages[32]. With this, our results foreshadow conceptually new domain-wall
274 applications that go beyond conducting 2D channels that can be written, moved, and
275 erased on demand. This opportunity brings us an important step closer to the realization
276 of reconfigurable *all-domain-wall* circuits for next-generation nanotechnology.

277

278 **References**

279 1. Salje, E. K. H. Multiferroic domain boundaries as active memory devices:
280 Trajectories towards domain boundary engineering. Chem. Phys. Chem. **11**, 940 -
281 950 (2010).
282 2. Catalan, G., Seidel, S., Ramesh, R., & Scott J. F. Domain wall nanoelectronics. Rev.
283 Mod. Phys. **84** 119 (2012).
284 3. Meier, D. Functional multiferroic domain walls in multiferroics. J. Phys.: Condens.
285 Matter 27, 463003 (2015).
286 4. Seidel, J. *et al.* Conduction at domain walls in oxide multiferroics. Nat. Mater. **8**,
287 229 – 234 (2009).

288 5. Maksymovych, P. *et al.* Tunable metallic conductance in ferroelectric
289 nanodomains. Nano Lett. **12**, 209 – 213 (2012).
290 6. Schröder, M. *et al.* Conducting domain walls in Lithium Niobate single crystals.
291 Adv. Funct. Mater. **22**, 3936 – 3944 (2012).
292 7. Sluka, T. *et al.* Free-electron gas at charged domain walls in insulating $BaTiO_3$,
293 Nat. Commun. **4**, 1808 (2013).
294 8. Meier, D. *et al*. Anisotropic conductance at improper ferroelectric domain walls.
295 Nat. Mater. **11**, 284 – 288 (2012).
296 9. Wu, W., Horibe, Y., Lee, N., Cheong, S.-W. & Guest, J. R. Conduction of
297 topologically protected charged ferroelectric domain walls. Phys. Rev. Lett. **108**,
298 077203 (2012).
299 10. Oh, Y. S., Luo, X., Huang, F.-T., Wang, Y., & Cheong, S.-W. Experimental
300 demonstration of hybrid improper ferroelectricity and the presence of abundant
301 charged walls in $(Ca,Sr)_3Ti_2O_7$ crystals. Nat. Mater. 14, 407 – 413 (2015)
302 11. Eliseev, E. A., Morozovska, A. N., Svechnikov, G. S., Gopalan, V. & Shur, V. Ya.
303 Static conductivity of charged domain walls in uniaxial ferroelectric
304 semiconductors. Phys. Rev. B **83**, 235313 (2011).
305 12. Gureev, M. Y., Tagantsev, A. K. & Setter, N. Head-to-head and tail-to-tail 180◦
306 domain walls in an isolated ferroelectric. Phys. Rev. B **83**, 184104 (2011).
307 13. Ma, E. Y. *et al*. Mobile metallic domain walls in an all-in-all-out magnetic
308 insulator. Science **350**, 538 – 541 (2015).

309 14. Campbell, M. P. *et al*. Hall effect in charged conducting domain walls. Nature
310 Commun. **7**, 13764 (2016).
311 15. Tselev, A. *et al*. Microwave a.c. conductivity of domain walls in ferroelectric thin
312 films. Nature Commun. **7**, 11630 (2016).
313 16. Ruff, E. *et al*. Conductivity contrast and tunneling charge transport in the vortex-
314 like ferroelectric domain pattern of multiferroic hexagonal $YMnO_3$. Phys. Rev.
315 Lett. **118**, 036803 (2017).
316 17. Schaab, J. *et al.* , Imaging and characterization of conducting ferroelectric
317 domain walls by photoemission electron microscopy. Appl. Phys. Lett. **104**,
318 232904 (2014).
319 18. Schaab, J., *et al*. Contact-free mapping of electronic transport phenomena of
320 polar domains in $SrMnO_3$ thin films, Phys. Rev. Appl. 5, 054009 (2016)
321 19. Kalashnikova, A. M. & Pisarev, R. V., Electronic structure of hexagonal rare-earth
322 manganites $RMnO_3$, JETP **78**, 143-147 (2003).
323 20. Chae, S. C. *et al*. Direct observation of the proliferation of ferroelectric loop
324 domains and vortex-antivortex Pairs. Phys. Rev. Lett. **108**, 167603 (2012).
325 21. Zhang, Q. H. *et al*. Direct observation of interlocked domain walls in hexagonal
326 $RMnO_3$ (R =Tm, Lu). Phys. Rev. B **85**, 020102(R) (2012).
327 22. Kumagai, Y. & Spaldin, N. A., Structural domain walls in polar hexagonal
328 manganites. Nat. Commun. **4**, 1540 (2012).
329 23. Choi *et al*. Insulating interlocked ferroelectric and structural antiphase domain
330 walls in multiferroic $YMnO_3$. Nature Mater. **9**, 253 – 258 (2010).

331 24. Skjærvø *et al*., Interstitial oxygen as a source of p-type conductivity in hexagonal
332 manganites, Nature Commun. 7, 13745 (2016).
333 25. Yan, Z. *et al*. Growth of High-quality hexagonal $ErMnO_3$ single-crystals by the
334 pressurized floating-zone method. J. Cryst. Growth **409**, 75 – 79 (2015).
335 26. Crassous, A., Sluka, T., Tagantsev, A. K., & Setter, N. Polarization charge as a
336 reconfigurable quasi-dopant in ferroelectric thin films. Nat. Nano. 10, 614 – 618
337 (2015).
338 27. Mundy, J. A. *et al*. Visualizing the interfacial evolution from charge compensation
339 to metallic screening across the manganite metal–insulator transition. Nat.
340 Commun. **5**, 3464 (2014).
341 28. Coeuré, Ph., Guinet, F., Peuzin, J. C., Buisson, G. & Bertaut, E. F. Ferroelectric
342 properties of hexagonal orthomanganites of yttrium and rare earths. Proc. Int.
343 Meet. Ferroelectr. **1**, Prague (1966).
344 29. Medvedeva, J. E., Anisimov, V. I., Korotin, M. A., Mryasov, O. N. & Freeman, A. J.
345 The effect of Coulomb correlation and magnetic ordering on the electronic
346 structure of hexagonal phases of ferroelectromagnetic $YMnO_3$, J. Phys.: Condens.
347 Matter **12,** 4947 – 4958 (2000).
348 30. Van Aken, B. B., Palstra, T. T. M., Filippetti, A. & Spaldin, N. A. The origin of
349 ferroelectricity in magnetoelectric $YMnO_3$. Nat. Mater. **3**, 164 – 170 (2004).
350 31. Rahmanizadeh, K., Wortmann, D., Bihlmayer, G. & Blügel, S. Charge and orbital
351 order at head-to-head domain walls in $PbTiO_3$. Phys. Rev. B **90**, 115104 (2014).

352 32. Fundamentals of Power Electronics, Second Edition, Erickson R. W. & Maksimovic, D. Springer Science + Business Media, LLC (2001).

354 33. Stengel, M., Fennie, C. J. & Ghosez, P. Electrical properties of improper ferroelectrics from first principles. Phys. Rev. B **86**, 094112 (2012).

356 34. Blöchl, P. E. Projector augmented-wave method. Phys. Rev. B **50**, 17953 – 17979 (1994).

358 35. Kresse, G. & Furthmüller, J. Efficient iterative schemes for ab initio total-energy calculations using a plane-wave basis set. Phys. Rev. B **54**, 11169 – 11186 (1996).

360 36. Perdew, J. P. & Zunger, A. Self-interaction correction to density-functional approximations for many-electron systems. Phys. Rev. B **23**, 5048 – 5079 (1981).

362 37. Liechtenstein, A. I., Anisimov, V. I. & Zaanen, J. Density-functional theory and strong interactions: Orbital ordering in Mott-Hubbard insulators. Phys. Rev. B **52**, R5467 – R5470 (1995).

365 38. Kumagai, Y. & Oba, F. Electrostatics-based finite-size corrections for first-principles point defect calculations. Phys. Rev. B **89**, 195205 (2014).

367

368 **Methods:**

369 **Spectroscopy:** $ErMnO_3$ platelets were oriented by Laue diffraction diffraction such that
370 the specimen would be imaged down the [100] zone axis of the crystal in TEM. Cross-
371 sectional TEM samples were prepared using an FEI Strata 400 Focused Ion Beam with a
372 final milling step of 2 keV to minimize surface damage. The TEM specimens were imaged
373 on a 100 keV Nion UltraSTEM optimized for EELS imaging (30 mrad convergence angle,

374 130 pA of usable beam current, ~ 1 Å spatial resolution). The microscope was equipped
375 with a Gatan Quantum Dual EELS spectrometer; EELS spectra were collected with a 0.1
376 eV/pixel dispersion resulting in 0.3 eV energy resolution. Fine structure information
377 from the O-K edge and $Mn\text{-}L_{2,3}$ edge was collected simultaneously with the ADF signal.
378 Gain and dark noise were corrected using Digital Micrograph™. Four cross-sectional TEM
379 specimens were prepared from two distinct $ErMnO_3$ platelets (within the platelets the
380 sample locations were separated by millimeters). Multiple distinct domain walls were
381 identified in each TEM specimen each separated by several microns. In sum, over a
382 dozen domain walls were analyzed. Post-acquisition, an off-line drift correction was
383 performed to correct the small sample drift (<0.5 Å/min). The $Mn\text{-}L_{2,3}$ fine structure was
384 analyzed following a standard power law background subtraction from approximately
385 10 eV prior to the edge onset. No additional noise reduction algorithms were employed
386 to avoid artifacts. Scanning was performed in rapid succession perpendicular to the wall
387 orientation so that each scan included signal from across the wall as well as the
388 reference regions on either side. Signals were binned perpendicular to the scan
389 direction to produce a single line scan through the wall. Manganese positions were
390 identified from the integrated signal intensity; the signal was then summed over each
391 manganese position to produce a single spectrum from each row of manganese atoms
392 in the spectrum image. Averaging over manganese positions increased the signal to
393 noise for the EELS analysis.

394 **Model Calculations:** In our semi-classical model of the carrier redistribution at the
395 charged domain walls, we treat the bulk material as a p-type semiconductor using the

396 calculated density of states (DOS) and values of P = 7.1 μC/cm^2 and ε = 13[33] extracted
397 from DFT calculations of bulk $YMnO_3$. The domain walls are introduced as charged
398 planes, with a surface charge density equal to $\pm 2P_z$. The equilibrium distribution of
399 screening carriers is calculated by iteratively solving the Poisson equation of a one-
400 dimensional system with two isolated domain walls. The local carrier density is
401 determined at each step by integrating the bulk DOS to the trial Fermi level, and by
402 enforcing the condition of overall charge neutrality.

403 **Density functional theory:** First-principles calculations were performed using the
404 projector augmented-wave method[34] as implemented in VASP[35]. PAW data sets with
405 radial cutoffs of 1.48, 1.22 and 0.80 Å for Y, Mn and O, respectively, were employed. The
406 exchange-correlation interactions between electrons were treated using the local
407 density approximation with Hubbard U correction[36,37]. The U and J parameters on the
408 Mn-3d orbitals were set to 5 and 0.88 eV, respectively. The $P6_3cm$ noncollinear magnetic
409 configuration of $YMnO_3$, which gives a band gap of 1.8 eV close to the experimental gap
410 of 1.6 eV[19] was adopted. Lattice constants and internal positions were fully relaxed until
411 the stress and forces acting on all atoms converged to less than 0.02 GPa and 0.005
412 eV/Å, respectively. The cutoff energy was set to 550 eV, and a Γ centered 4 × 4 × 2 k-
413 point sampling for the reciprocal space integration was employed. The projected
414 densities of states were evaluated within the spheres centered on the atomic sites with
415 radii of 1.82, 1.32, and 0.82 Å for Y, Mn, and O, respectively. For the calculations of
416 polarons, the lattice constants were fixed to the values of the relaxed unit cell, and a Γ
417 centered 2 × 2 × 2 k-point sampling was adopted. The local symmetry was reduced by

418 moving the apical oxygen ions away from the Mn ion by 0.2 Å so that an electron can
419 easily be captured to the Mn-d_{z^2} orbital. Y ions were not moved in the initial structure,
420 but they were spontaneously relaxed to the lowest energy positions via structure
421 optimization. Relative energies between the polaronic and itinerant Bloch electrons
422 were calculated for 2 × 2 × 1 supercells composed of 120 atoms as a function of the *U*
423 parameter, with *J* fixed at 0.88 eV. For itinerant electrons, band-filling corrections were
424 applied. In order to remove the spurious electrostatic energy caused by the finite
425 background charge, we adopted the scheme of ref. 38.

426 **Data availability.** The data that support the findings of this study are available from the
427 authors on reasonable request.

428 **Supplementary Information** is linked to the online version of the paper at
429 www.nature.com/nature.

430

431 **Acknowledgement:** We thank M. Fiebig for direct financial support and scientific input,
432 M. Trassin and A. Kaiser for fruitful discussions. We thank HZB for the allocation of
433 synchrotron beam time and we thankfully acknowledge financial support by HZB. D.M.,
434 J.S. and N.A.S. acknowledge funding from the ETH Zürich and the SNF (proposal Nr.
435 200021_149192, D.M. and J.S.), the Alexander von Humboldt Foundation (D.M.) and the
436 ERC Advanced Grant program (grant number 291151, N.A.S.). Electron microscopy
437 research at Cornell (J.A.M., M.E.H., D.A.M. and D.G.S.) was supported by the U.S.
438 Department of Energy, Office of Basic Energy Sciences, Division of Materials Sciences

439 and Engineering under Award #DE-SC0002334. This work made use of the electron
440 microscopy facility of the Cornell Center for Materials Research (CCMR) with support
441 from the National Science Foundation Materials Research Science and Engineering
442 Centers (MRSEC) program (DMR-1120296) and NSF IMR-0417392. We gratefully
443 acknowledge the use of facilities with the LeRoy Eyring Center for Solid State Science at
444 Arizona State University and assistance from J. Mardinly and T. Aoki. J.A.M.
445 acknowledges financial support from the Army Research Office in the form of a National
446 Defense Science & Engineering Graduate Fellowship and from the National Science
447 Foundation in the form of a National Science Foundation Graduate Research Fellowship.
448 M.S. was supported by MINECO-Spain through Grants No. FIS2013-48668-C2-2-P and No.
449 SEV-2015-0496, and Generalitat de Catalunya (2014 SGR301). E.B. and Z.Y. were
450 supported in part by the U.S. Department of Energy and carried out at the Lawrence
451 Berkeley National Laboratory under Contract No. DE-AC02-05CH11231.

452

453 **Author Contributions:** J.A.M. and M.E.H. conducted and analyzed the EELS
454 measurements, assisted by R.H., under supervision of D.A.M. and D.G.S. Y.K., M.S. and
455 N.A.S. performed the semiclassical and DFT calculations. J.S. performed the cAFM
456 measurements under supervision of D.M. The analysis in terms of X-PEEM was provided
457 by I.P.K., J.S., D.M.G., H.D., C.M.S. and D.M.; Z.Y., E.B. and R.R. allocated the samples.
458 A.C. and D.M. developed the concept of electric-field gating. D.M. initiated and

459 coordinated this project, and wrote the manuscript supported by J.A.M., Y.K., M.S., A.C.
460 and N.A.S.

461 Author Information: Reprints and permission information is available at
462 www.nature.com/reprints. The authors declare no competing financial interests.

463

464

465 ## Figure Captions

466 **Figure 1 | Electronic transport and band structure at tail-to-tail and head-to-head**
467 **walls. a,** cAFM scan obtained at a bias voltage of 2.5 V on $ErMnO_3$ with in-plane
468 polarization as indicated by the white arrows (the orientation corresponds to a y-cut
469 with the (110)-direction normal to the sample surface). The image reveals a sixfold
470 meeting point of conducting tail-to-tail (bright) and insulating head-to-head (dark)
471 domain walls. **b,** cAFM image obtained with a bias voltage of 6V at the same position as
472 shown in 1a with both tail-to-tail and head-to-head walls exhibiting enhanced
473 conductance compared to the bulk. **c,** Relative current-voltage characteristics measured
474 at tail-to-tail and head-to-head walls after subtraction of the bulk current (for reference,
475 the bulk conductance is shown in the inset). See Supplementary Fig. S3 for
476 corresponding spatially resolved data. **d,** Calculated band bending at tail-to-tail and
477 head-to-head domain walls (vertical dashed lines) with arrows indicating the
478 polarization orientation in adjacent domains. Black solid lines correspond to the

479 conduction band minimum (CBM) and valence band maximum (VBM) for $p_0 = 2 \cdot 10^{19}$

480 cm^{-3} with the horizontal dashed line indicating the Fermi level, E_{Fermi}. **e,** Calculated

481 carrier density at head-to-head walls. With increasing hole carrier density the screening

482 by hole depletion becomes more efficient so that the density of electrons decreases.

483 The inset presents the average carrier density. Lines are running averages based on a

484 Gaussian convolution function ($\propto \exp(-x^2/s^2)$, s = 30 nm), which corresponds to a

485 realistic spatial resolution when mapping local current by cAFM. **f,** Conceptual sketch of

486 a domain-wall-based field-effect transistor with polarization charges playing the role of

487 the gate.

488 **Figure 2 | Manganese valence change at head-to-head domain walls. a**, HAADF-STEM

489 image of a head-to-head domain wall. The image is colored to indicate the magnitude

490 and direction of the displacement of erbium atoms with a sharp transition between +*P*

491 and –*P* domains (–*P* domain: up-down-down; +*P* domain: down-up-up as indicated by

492 yellow circles)[21]. The scale bar is 1 nm. **b**, Layer-by-layer EELS spectra showing the

493 evolution of the Mn $L_{2,3}$-edge across the head-to-head domain wall. **c**, Zoom-in to the L_3-

494 edge in **b**. A comparison of the EELS spectra (blue dots) with Mn^{3+} reference data (solid

495 line) reveals a spectral feature around 641 eV (indicated by the dashed line) that occurs

496 in the vicinity of the head-to-head domain wall. **d**, Electron transfer (per manganese

497 atom at the domain wall) to the wall calculated from the local manganese valence

498 measured by EELS. Error bars are the standard error of the mean.

499 **Figure 3 | Orbital nature of electrons at head-to-head domain walls. a**, Orbital-resolved
500 density of states (DOS). The black lines indicate the sum of the local density of states,
501 while the blue and red lines show the contributions from the different orbitals. The
502 black dashed line at 0 eV indicates the Fermi energy. O_{ap} and O_{ip} represent the oxygens
503 located at the apical sites and in-plane sites, respectively, of the MnO-bipyramidal layers.
504 **b**, Calculated relative energy between electronic Bloch and polaron states. Data points
505 (black crosses) above the dashed line indicate that an itinerant Bloch state is stable for
506 the respective *U* values, whereas data points below the line show that a polaronic state
507 is stabilized. **c**, Illustration of the calculated electronic polaron state.

508 **Figure 4 | Electric-field control of electronic transport at head-to-head domain walls. a,**
509 Normalized domain-wall current measured as a function of time over 20 switching
510 cycles between resistive ($I_0 < I_{bulk}$) and conducting ($I_1 > I_{bulk}$) behavior. For voltages V_0 =
511 2V and ΔV = 3V (see inset to 4a for a schematic illustration) , reversible control can be
512 reliably realized for 20 switching cycles, which is the largest number of cycles we
513 investigated. **b,** Enhanced gain can be achieved, e.g., by increasing I_0, yielding $\Delta I / \Delta V \approx$
514 15 pA V^{-1} for V_0 = 4V and ΔV = 1V. The increase in gain, however, requires larger
515 currents which cause degradation as described in the main text. **c,** Sketch showing the
516 conductive domain-wall state for $V = V_0 + \Delta V$ with itinerant electrons illustrated in blue.
517 **d,** Resistive domain-wall state with localized electrons for V_0.

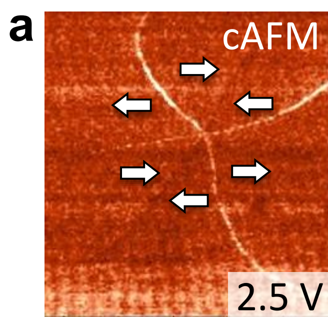

a
cAFM
2.5 V

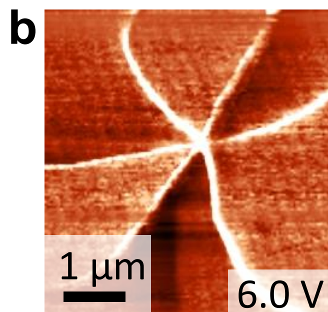

b
1 µm
6.0 V

c
Relative conductance (pA)
Voltage (V)
Bulk
Bulk conductance (pA)
Voltage (V)

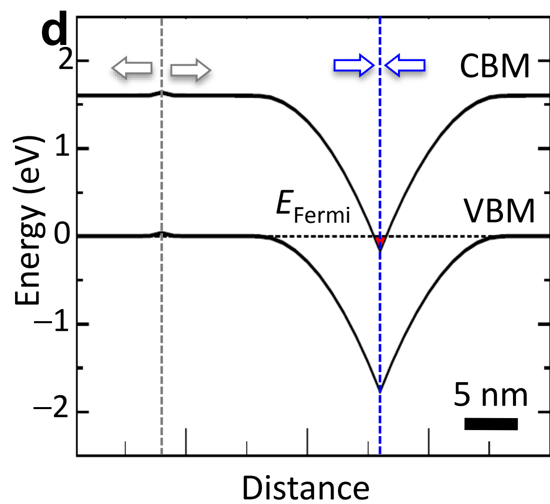

d
Energy (eV)
CBM
VBM
E_{Fermi}
5 nm
Distance

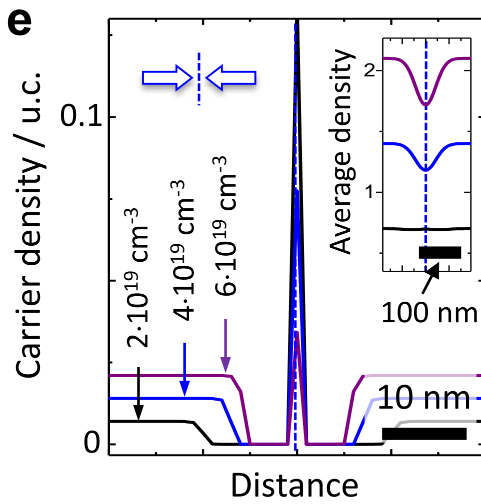

e
Carrier density / u.c.
$2\cdot10^{19}$ cm^{-3}
$4\cdot10^{19}$ cm^{-3}
$6\cdot10^{19}$ cm^{-3}
Average density
100 nm
10 nm
Distance

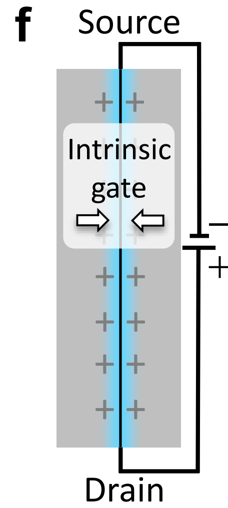

f
Source
Intrinsic gate
Drain

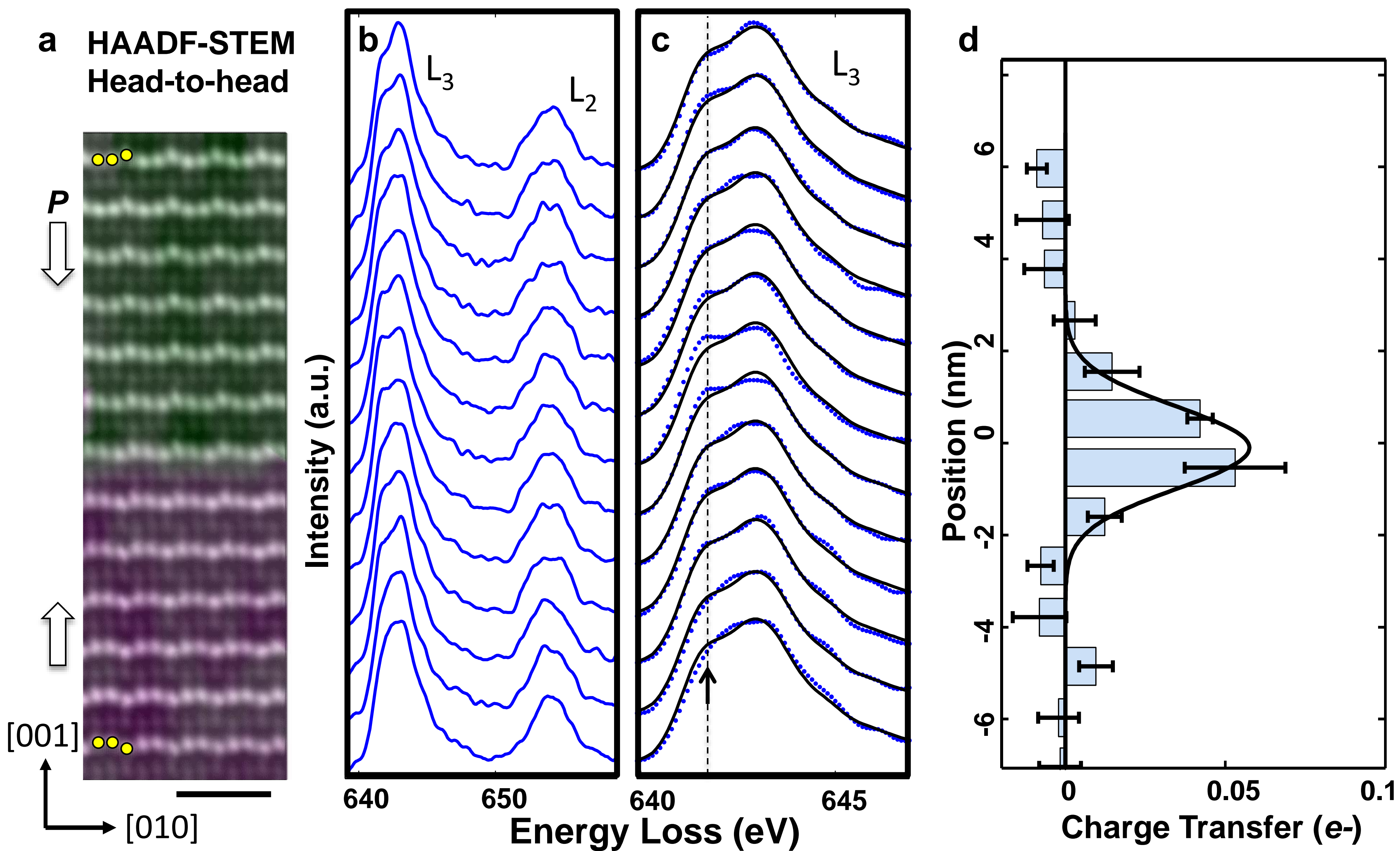

a
HAADF-STEM
Head-to-head
P
[001]
[010]
b
L3
L2
c
L3
d
Intensity (a.u.)
640
650
640
645
Energy Loss (eV)
Position (nm)
6
4
2
0
-2
-4
-6
0
0.05
0.1
Charge Transfer (e-)

a
total
Y
Mn
$d_{xy}+d_{x2-y2}$
d_{z2}
O_{ap}
p_x+p_y
p_z
O_{ip}
p_x+p_y
p_z
DOS (1/eV/unit-cell)
Energy (eV)

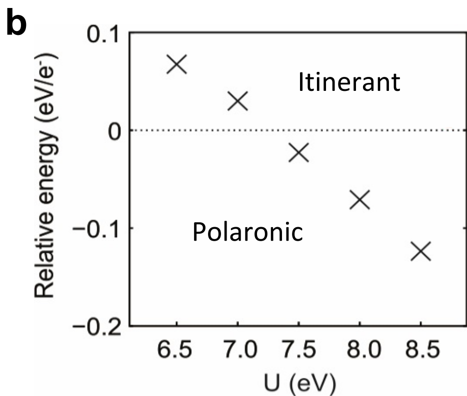
b
Relative energy (eV/e⁻)
Itinerant
Polaronic
U (eV)

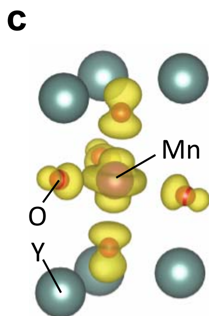
c
Mn
O
Y

a

Wall

Input

Output

$\equiv$

I_1

I_0

V_0

$V_0 + \Delta V$

$\frac{1}{\Delta V}\frac{\Delta I}{I_{\mathrm{bulk}}}\ (V^{-1})$

1.5

1.0

0.5

0.0

-0.5

$\Delta V = 3$ V

0 10 20 30 40

t (s)

b

$\Delta V = 1$ V

0 2 4

t (s)

c

Itinerant

P

$V_0 + \Delta V$

d

Localized

e

P

V_0